



# Outer Membrane *c*-Type Cytochromes OmcA and MtrC Play Distinct Roles in Enhancing the Attachment of *Shewanella oneidensis* MR-1 Cells to Goethite

Xinxin Jing,<sup>a</sup>  Yichao Wu,<sup>a</sup> Liang Shi,<sup>b,c</sup> Caroline L. Peacock,<sup>d</sup> Noha Mohamed Ashry,<sup>a,e</sup> Chunhui Gao,<sup>a</sup>  Qiaoyun Huang,<sup>a</sup>  Peng Cai<sup>a</sup>

<sup>a</sup>State Key Laboratory of Agricultural Microbiology, College of Resources and Environment, Huazhong Agricultural University, Wuhan, China

<sup>b</sup>Department of Biological Sciences and Technology, School of Environmental Studies, China University of Geosciences, Wuhan, China

<sup>c</sup>State Key Laboratory of Biogeology and Environmental Geology, China University of Geosciences, Wuhan, China

<sup>d</sup>School of Earth and Environment, University of Leeds, Leeds, United Kingdom

<sup>e</sup>Agriculture Microbiology Department, Faculty of Agriculture, Benha University, Moshthohor, Qalubia, Egypt

Xinxin Jing and Yichao Wu contributed equally to this work. Author order was determined by level of contribution.

**ABSTRACT** The outer membrane *c*-type cytochromes (*c*-Cyts) OmcA and MtrC in *Shewanella* are key terminal reductases that bind and transfer electrons directly to iron (hydr)oxides. Although the amounts of OmcA and MtrC at the cell surface and their molecular structures are largely comparable, MtrC is known to play a more important role in dissimilatory iron reduction. To explore the roles of these outer membrane *c*-Cyts in the interaction of *Shewanella oneidensis* MR-1 with iron oxides, the processes of attachment of *S. oneidensis* MR-1 wild type and *c*-type cytochrome-deficient mutants (the  $\Delta omcA$ ,  $\Delta mtrC$ , and  $\Delta omcA \Delta mtrC$  mutants) to goethite are compared via quartz crystal microbalance with dissipation monitoring (QCM-D). Strains with OmcA exhibit a rapid initial attachment. The quantitative model for QCM-D responses reveals that MtrC enhances the contact area and contact elasticity of cells with goethite by more than one and two times, respectively. *In situ* attenuated total reflectance Fourier transform infrared two-dimensional correlation spectroscopic (ATR-FTIR 2D-CoS) analysis shows that MtrC promotes the initial interfacial reaction via an inner-sphere coordination. Atomic force microscopy (AFM) analysis demonstrates that OmcA enhances the attractive force between cells and goethite by about 60%. As a result, OmcA contributes to a higher attractive force with goethite and induces a rapid short-term attachment, while MtrC is more important in the longer-term interaction through an enhanced contact area, which promotes interfacial reactions. These results reveal that *c*-Cyts OmcA and MtrC adopt different mechanisms for enhancing the attachment of *S. oneidensis* MR-1 cells to goethite. It improves our understanding of the function of outer membrane *c*-Cyts and the influence of cell surface macromolecules in cell-mineral interactions.

**IMPORTANCE** *Shewanella* species are one group of versatile and widespread dissimilatory iron-reducing bacteria, which are capable of respiring insoluble iron minerals via six multiheme *c*-type cytochromes. Outer membrane *c*-type cytochromes (*c*-Cyts) OmcA and MtrC are the terminal reductases in this pathway and have comparable protein structures. In this study, we elucidate the different roles of OmcA and MtrC in the interaction of *S. oneidensis* MR-1 with goethite at the whole-cell level. OmcA confers enhanced affinity toward goethite and results in rapid attachment. Meanwhile, MtrC significantly increases the contact area of bacterial cells with goethite and promotes the interfacial reaction, which may explain its central role in extracellular electron transfer. This study provides novel insights into the role of bacterial surface macromolecules in the interfacial interaction of bacteria with minerals,

**Citation** Jing X, Wu Y, Shi L, Peacock CL, Ashry NM, Gao C, Huang Q, Cai P. 2020. Outer membrane *c*-type cytochromes OmcA and MtrC play distinct roles in enhancing the attachment of *Shewanella oneidensis* MR-1 cells to goethite. *Appl Environ Microbiol* 86:e01941-20. <https://doi.org/10.1128/AEM.01941-20>.

**Editor** Shuang-Jiang Liu, Chinese Academy of Sciences

**Copyright** © 2020 American Society for Microbiology. All Rights Reserved.

Address correspondence to Peng Cai, cp@mail.hzau.edu.cn.

**Received** 7 August 2020

**Accepted** 12 September 2020

**Accepted manuscript posted online** 25 September 2020

**Published** 10 November 2020

which is critical to the development of a comprehensive understanding of cell-mineral interactions.

**KEYWORDS** *Shewanella oneidensis*, outer-membrane *c*-type cytochromes, attachment, iron oxide, QCM-D

**M**icrobial dissimilatory iron reduction (DIR) plays an important role in soil and sediment biogeochemistry (1). Under oxic conditions, iron is largely present as ferric iron, which at typical soil and sediment pH is precipitated as iron (hydr)oxide minerals (2). Under anoxic conditions, these (hydr)oxides can serve as terminal electron acceptors and are thus reduced to ferrous iron species, coupled to the oxidation of organic carbon (1). This redox process mediates the biogeochemical cycling of iron and carbon but also impacts the reactivity and cycling of other essential bioelements and contaminants, through the control of subsurface redox conditions (3).

Although microbial cell envelopes are impermeable to iron minerals, microbes have evolved various mechanisms to facilitate extracellular electron transfer (4, 5). *Shewanella* species are one group of versatile and widespread metal (hydr)oxide-reducing bacteria which are capable of respiring insoluble iron minerals via six multiheme *c*-type cytochromes (6). These cytochromes, located in membranes and periplasmic space, transfer electrons across the cell envelope to mineral surfaces. Outer membrane *c*-type cytochromes (*c*-Cyts) OmcA and MtrC are the terminal reductases in this pathway that contact and exchange electrons with extracellular minerals directly. When lacking these outer membrane *c*-Cyts, *S. oneidensis* MR-1 is unable to proliferate on iron mineral surfaces under anoxic conditions (7, 8).

Due to the indispensable role of outer membrane *c*-Cyts in extracellular electron transfer, both their distribution and structure at cell surfaces and their interaction with iron (hydr)oxides have been studied. In particular, previous works have shown that there are similar amounts of MtrC and OmcA present on *S. oneidensis* MR-1 cell surfaces (9, 10), but antibody recognition suggests that MtrC is uniformly distributed across the cell surfaces, while OmcA is localized mainly at the cell-mineral interface (11). Furthermore, OmcA and MtrC are reported to contain similar structural and heme arrangements (4, 12). In order to transfer electrons to minerals directly, OmcA and MtrC contain a conserved binding motif (Ser/Thr-Pro-Ser/Thr) via which hydrogen bonds form between serine residues and hydroxylated iron (hydr)oxide surfaces (13). The crystal structure of OmcA places the binding motif near heme 10, which brings the electron egress site to about 10 Å of the mineral surface (14). Accordingly, force measurements with atomic force microscopy (AFM) reveal that the strength of the bond between OmcA and hematite is approximately twice as strong as that of the MtrC-hematite bond (15).

Although the amounts of OmcA and MtrC at the cell surface and their protein structures are reportedly largely comparable, their functions during cell-mineral interactions appear to be different. In this regard, most studies to date have used purified *c*-Cyts to elucidate the role of outer membrane *c*-Cyts in bacterium-mineral interactions (9, 14–18), but a limited number of studies with whole cells of *S. oneidensis* MR-1 reveal that the mutant strain lacking MtrC is less able to reduce iron (hydr)oxide than strains lacking OmcA, which suggests that MtrC plays a more dominant role than OmcA in extracellular electron transfer and iron (hydr)oxide reductive dissolution (8, 19, 20). Although their different contributions to extracellular electron transfer may be attributed to the close association of MtrC to the transmembrane complex MtrAB, the potentially different roles of OmcA and MtrC in the attachment of *Shewanella* cells onto iron oxides at the whole-cell level remain largely unknown.

The objective of this study was to explore the roles of *c*-Cyts (OmcA and MtrC) in the interaction of *S. oneidensis* MR-1 with the common soil and sediment iron (hydr)oxide goethite. A quartz crystal microbalance with dissipation monitoring (QCM-D) was used to compare the dynamic attachment processes of *S. oneidensis* MR-1 wild-type (WT) and mutant strains with outer membrane *c*-type cytochromes deleted (lacking OmcA [the

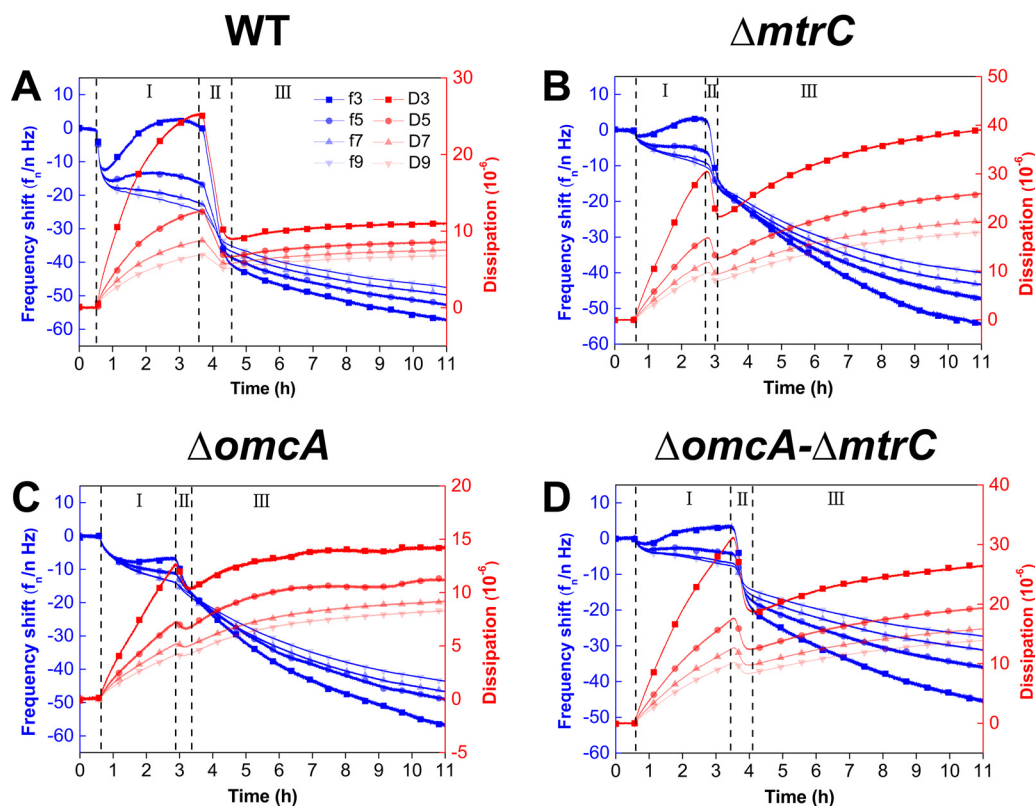


**FIG 1** The frequency ( $\Delta f$ ) and dissipation ( $\Delta D$ ) shifts for the attachment of the WT (A) and the  $\Delta mtrC$  (B),  $\Delta omcA$  (C), and  $\Delta omcA \Delta mtrC$  (D) mutants on goethite-coated QCM-D sensors. I, II, and III are different stages of bacterial attachment based on the changes of  $\Delta D$ .  $f_n$  and  $D_n$  indicate the frequency and dissipation, respectively, at four different overtones.

$\Delta omcA$  mutant], MtrC [the  $\Delta mtrC$  mutant], or both OmcA and MtrC [the  $\Delta omcA \Delta mtrC$  mutant]). The QCM-D responses were fitted to a quantitative model to describe the underlying mechanical properties of attachment. Molecular-level processes were characterized by using attenuated total reflectance Fourier transform infrared (ATR-FTIR) spectroscopy. Atomic force microscopy (AFM) analysis was further employed to examine the direct interaction force between *S. oneidensis* MR-1 and goethite. This study provides novel insights into the role of bacterial surface macromolecules in the interfacial interaction of bacteria with minerals, which is critical for the development of a comprehensive understanding of cell-mineral interactions and how they help control subsurface redox and biogeochemical conditions.

## RESULTS

**QCM-D attachment behavior of *S. oneidensis* MR-1 to goethite.** QCM-D was used to investigate the role of outer membrane *c*-Cyts in the dynamics of *S. oneidensis* MR-1 attachment to goethite. Upon introduction of bacterial cells to the goethite surface, the dissipation shift ( $\Delta D$ ) initially increases rapidly during the first 3 h of attachment, decreases rapidly during the next 1 h of attachment, and then gradually approaches a constant value after 4 h of attachment (Fig. 1). Based on the changes in  $\Delta D$ , the entire attachment process can be divided into three stages.

In the first stage,  $\Delta D$  values of both the WT and the mutants increase but the frequency shifts ( $\Delta f$ ) differ between different strains, especially at the 3rd overtone ( $\Delta f_3$ ) (Fig. 1). Specifically, the  $\Delta f_3$  values of the WT (Fig. 1A) and the mutant lacking MtrC ( $\Delta mtrC$ ) (Fig. 1B) decrease and then increase gradually, reaching a peak with increasing  $\Delta D$ . This trend in  $\Delta f_3$  indicates that there is considerable bacterial attachment. Meanwhile, there are negligible changes in  $\Delta f$  for the mutant lacking OmcA ( $\Delta omcA$ ) and that lacking both OmcA and MtrC ( $\Delta omcA \Delta mtrC$ ), indicating that there is less bacterial

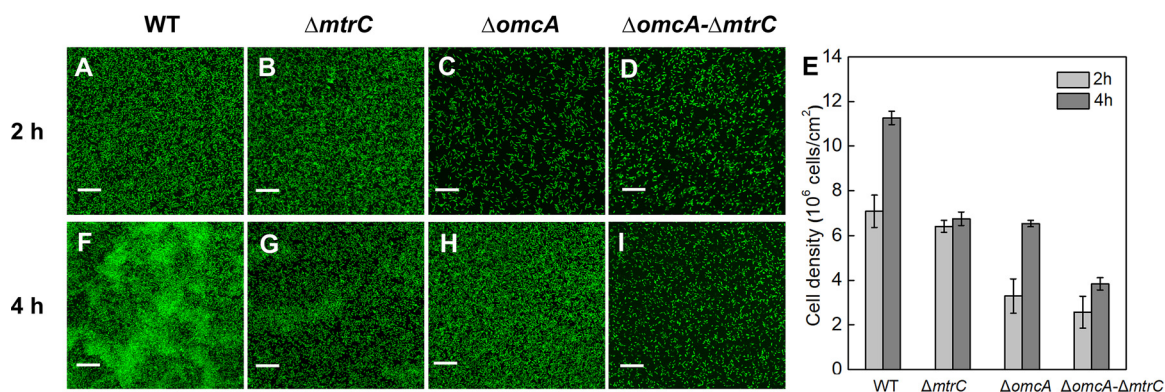


**FIG 2** WT (A, F),  $\Delta mtrC$  mutant (B, G),  $\Delta omcA$  mutant (C, H), and  $\Delta omcA \Delta mtrC$  mutant (D, I) after 2 and 4 h of attachment to goethite surfaces. (E) Surface cell density determined by statistical image analysis. The scale bar represents 20  $\mu\text{m}$ .

attachment (Fig. 1C and D). These results agree with the microscope images in that the WT and the  $\Delta mtrC$  mutant have comparable amounts of attached cells at the end of the first stage [ $(7.1 \pm 0.7) \times 10^6$  versus  $(6.4 \pm 0.3) \times 10^6$  cells/cm<sup>2</sup>] (Fig. 2), but the  $\Delta omcA$  and  $\Delta omcA \Delta mtrC$  mutants have significantly fewer attached cells, the surface cell densities of which are less than 50% of that of the WT ( $P < 0.01$ ). It should be noted that although an increased mass loading on the QCM sensor resulting from bacterial attachment to the goethite surface usually leads to a negative shift in  $\Delta f$ , a positive shift in  $\Delta f$  at the 3rd overtone is observed in the first stage for the WT and the  $\Delta mtrC$  mutant (Fig. 1). The positive shift in  $\Delta f$  is attributed to the oscillation of the soft bacterial layer, which counteracts the negative frequency shift (21, 22). As the sensing depth of QCM-D decays with  $1/\sqrt{n}$  (21), the positive shift in  $\Delta f_3$  and significantly increased  $\Delta D_3$  indicate that thick, soft bacterial layers of the WT and the  $\Delta mtrC$  mutant develop on the goethite surface.

In the second stage, when  $\Delta D$  reaches a peak after 3 h of attachment,  $\Delta D$  and  $\Delta f$  values of the WT and mutants start to decrease simultaneously (Fig. 1). This trend suggests that there is a transition in the type and number of bacterial attachments which may suppress the oscillation of the surface-associated cells and reduce the steric hindrance, thus facilitating further cell attachment. Based on confocal laser scanning microscopy (CLSM) imaging, all strains except the  $\Delta mtrC$  mutant show a substantial increase in the amount of attached cells (Fig. 2). At the end of the second stage, the  $\Delta omcA$  and  $\Delta mtrC$  mutants share similar surface cell densities [ $(6.5 \pm 0.1) \times 10^6$  versus  $(6.8 \pm 0.3) \times 10^6$  cells/cm<sup>2</sup>], which are significantly higher than that of the  $\Delta omcA \Delta mtrC$  mutant [ $(3.8 \pm 0.3) \times 10^6$  cells/cm<sup>2</sup>,  $P < 0.01$ ].

In the third stage,  $\Delta D$  and  $\Delta f$  gradually approach certain values (Fig. 1). Except for the  $\Delta omcA \Delta mtrC$  mutant, no significant increase in bacterial density on the goethite surface is observed (see Fig. S1 in the supplemental material). This indicates that stable bacterial attachment is established after about 4 h. The  $\Delta D$  and  $\Delta f$  values for the WT across different overtones converge to  $1 \times 10^{-5}$  and  $-50$  Hz, respectively, while the  $\Delta D$  and  $\Delta f$  values for mutants diverge (Fig. 1). As the penetration depth of the acoustic wave decays with the increase of overtones, the converged  $\Delta D$  and  $\Delta f$  values suggest that WT cells form a homogeneous layer on goethite (23). Regarding the mutant strains, the  $\Delta D$  value at the third overtone ( $\Delta D_3$ ) of the  $\Delta omcA$  mutant at 11 h is much lower than those of the  $\Delta mtrC$  and  $\Delta omcA \Delta mtrC$  mutants, which suggests a stable attachment with less oscillation.

**Modeled viscoelastic characteristics of *S. oneidensis* MR-1 attachment to goethite.** To further investigate the adhesive behavior of the surface-associated bacteria, the recorded  $\Delta f$  and  $\Delta D$  values at 10 h are fitted to the quantitative QCM-D model (24). The  $\Delta f$  values for the WT and the mutant lacking OmcA ( $\Delta omcA$ ) show a negative linear correlation with the overtone number (Fig. 3A and C), which suggests that the QCM-D signals are dominated by inertial response and can be well described by the free-

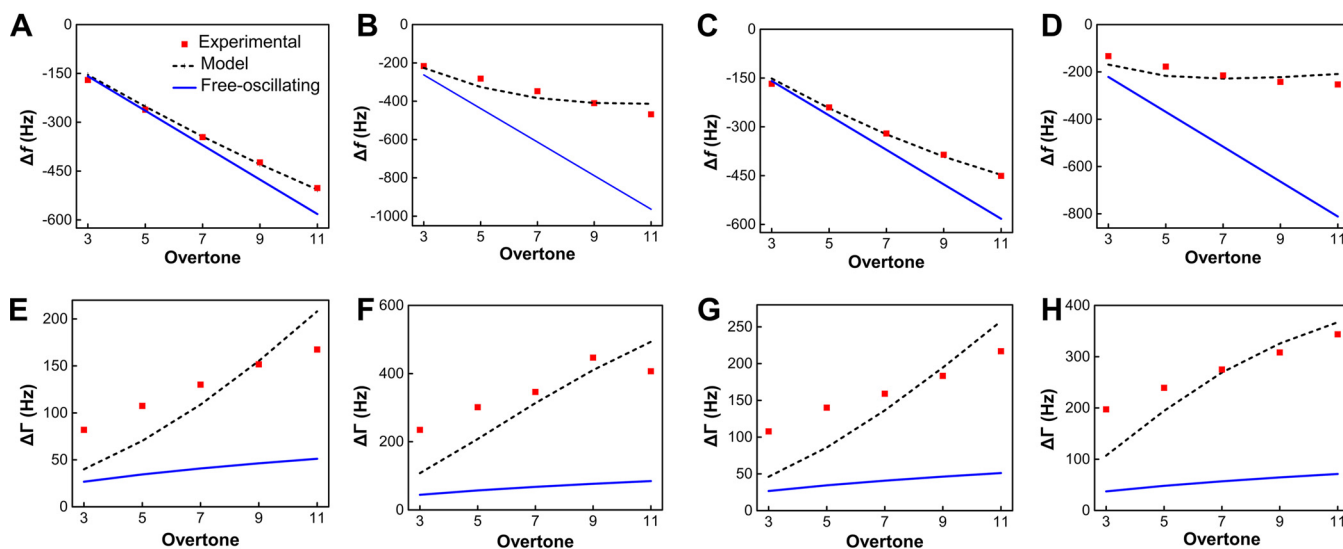


**FIG 3** Experimental and predicted  $\Delta f$  and  $\Delta \Gamma$  values as a function of the overtone number for the WT (A, E) and  $\Delta mtrC$  (B, F),  $\Delta omcA$  (C, G), and  $\Delta omcA \Delta mtrC$  (D, H) mutants.

oscillation model (Fig. 4, upper portion). As the inertial and elastic loads are connected in parallel (Fig. 4), the reciprocal of the total QCM-D response equals the sum of the reciprocals of inertial and elastic loads. Therefore, these inertial QCM-D responses suggest that there is a higher contribution from contact elasticity during bacterial attachment. In contrast, the  $\Delta f$  values of the mutant lacking MtrC ( $\Delta mtrC$ ) and that lacking both OmcA and MtrC ( $\Delta omcA \Delta mtrC$ ) deviate from the free-oscillation model, which suggests a nonnegligible contribution of inertial interaction (Fig. 3B and D). Based on model fitting, the contact elasticity parameter for the WT is the highest and is 48.7% higher than that for the  $\Delta omcA$  mutant (Table 1). The mutants lacking MtrC, i.e., the  $\Delta mtrC$  and  $\Delta omcA \Delta mtrC$  strains, demonstrate 71.4% and 82.0% reduction in contact elasticity, respectively, compared with the WT. These results indicate that the presence of MtrC contributes to elastic interactions between *S. oneidensis* MR-1 and goethite.

The bandwidth shift ( $\Delta \Gamma$ ) for all the strains exceeds the free-oscillation model prediction (Fig. 3E to H). This discrepancy suggests that the viscosity of the attached bacterial layer contributes significantly to energy dissipation. The positive relationship between  $\Delta \Gamma$  and the overtone number also highlights the involvement of viscous dissipation, which is expected to correlate with  $n^{1/2}$  (Fig. 4). The magnitude of the

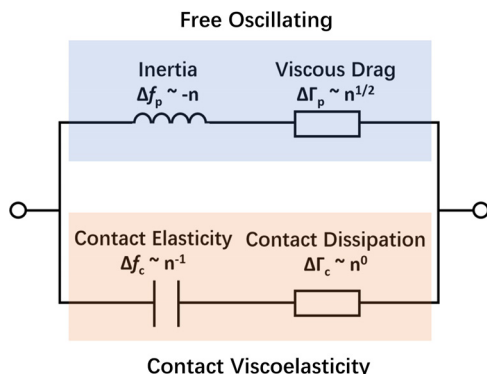


**FIG 4** Proposed equivalent circuits for the load impedance of the crystal associated with a single attached bacterial cell, showing the overtone dependence of inertial, viscous, elastic, and dissipative loads.



**TABLE 1** Fitted parameters for *Shewanella* attachment to goethite<sup>a</sup>

Strain	$\kappa_c$ (N m <sup>-1</sup> )	$\xi_c$ (10 <sup>-8</sup> Pa m s)	$N_p$ (10 <sup>5</sup> cm <sup>-2</sup> )	$r_c$ (nm)	$d$
WT	41.13 (41.11–41.15)	506.15 (481.39–539.51)	1.20 (1.19–1.22)	536.37 (536.27–536.45)	92.66
$\Delta mtrC$ mutant	11.76 (11.75–11.78)	150.96 (145.67–155.58)	1.99 (1.95–2.04)	353.39 (353.22–353.55)	266.15
$\Delta omcA$ mutant	27.67 (27.65–27.69)	336.42 (322.95–351.24)	1.21 (1.19–1.22)	469.99 (469.87–470.09)	112.79
$\Delta omcA \Delta mtrC$ mutant	7.40 (7.39–7.42)	101.17 (96.89–103.88)	1.68 (1.64–1.73)	302.79 (302.63–303.01)	178.39

<sup>a</sup> $\kappa_c$ , contact elasticity;  $\xi_c$ , contact damping;  $N_p$ , density of attached cells;  $r_c$ , radius of contact region for single attached cells;  $d$ , deviation. Ninety-five percent confidence regions of parameters are given in parentheses.

contact damping parameter follows the same sequence as the elastic coefficient  $\kappa_c$  (WT >  $\Delta omcA$  mutant >  $\Delta mtrC$  mutant >  $\Delta omcA \Delta mtrC$  mutant) (Table 1). This is consistent with recent work showing that a higher elastic coefficient is associated with higher damping parameters (24). The contact radius of individual attached cells can be further estimated based on the predicted parameters. The WT exhibits the highest contact radius, which reaches 536.37 nm (Table 1) and is more than 1.7-fold higher than that of the  $\Delta omcA \Delta mtrC$  mutant. Among the mutants, the contact radius of the  $\Delta omcA$  mutant is significantly higher than that of the  $\Delta mtrC$  mutant. These results suggest that the presence of MtrC enhances the contact area between *S. oneidensis* MR-1 and goethite and that a higher contact area results in higher elastic and damping effects during the cell-mineral interaction. The predicted result is consistent with the immunolocalization assay results. That assay shows that the distribution of MtrC and OmcA on the surface of the WT is uniform (Fig. 5A and B). When MtrC is lacking, the distribution of OmcA on the cell surface becomes heterogeneous. Manders' overlap coefficient (MOC) is calculated to evaluate the distribution of outer membrane *c*-Cyts. The overlap coefficient of OmcA in the  $\Delta mtrC$  mutant is 22% less than that of the WT, while the  $\Delta omcA$  mutant shares a comparable MOC with the WT. It should be noted that the predicted surface cell densities ( $N_p$ ) are 1 order of magnitude less than those determined from the microscope data (Table 1). The discrepancy may be caused by the small fraction of observed cells that formed a stable contact with the goethite surface (24).

**2D-CoS analysis of the interaction sequence of the bacterial cell surface functional groups on goethite.** The FTIR spectra of goethite-free *S. oneidensis* strains reveal prominent amide and phosphate bands, including bands at 1,081 cm<sup>-1</sup> [ $\nu_s(\text{PO}_2^-)$ ], 1,235 cm<sup>-1</sup> [ $\nu_{as}(\text{PO}_2^-)$ ], 1,543 cm<sup>-1</sup> (amide II), and 1,654 cm<sup>-1</sup> (amide I) ( $\nu_s$  indicates  $\text{PO}_2^-$  symmetric stretch, and  $\nu_{as}$  indicates  $\text{PO}_2^-$  asymmetric stretch) (Fig. S2 and Table S1). The spectral signatures of the WT and mutants are similar, which suggests that the

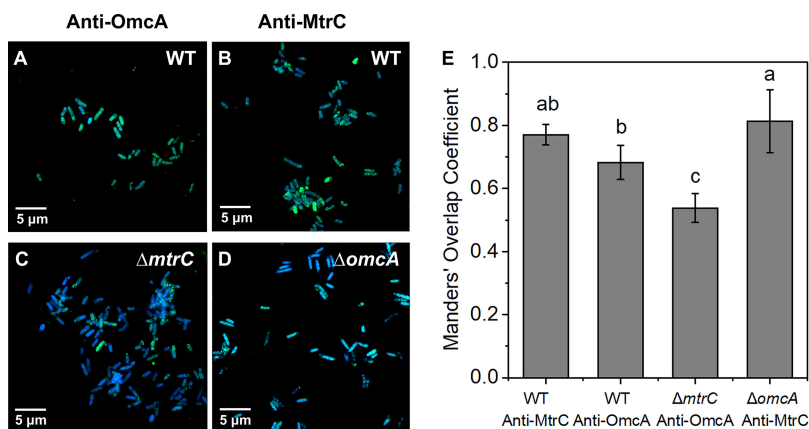


**FIG 5** Immunolocalization images of outer membrane *c*-Cyts OmcA and MtrC on cell surfaces of the WT (A, B) and  $\Delta mtrC$  (C) and  $\Delta omcA$  (D) mutant strains stained with DAPI (blue). Outer membrane *c*-Cyts OmcA and MtrC were specifically labeled with antibodies against OmcA (A and C) (green) or MtrC (B and D) (green). (E) Manders' overlap coefficient (MOC) of OmcA and MtrC on the WT,  $\Delta omcA$  mutant, and  $\Delta mtrC$  mutant surfaces.

absence of *c*-Cyts does not significantly affect the abundance of the different surface functional groups.

Online *in situ* ATR-FTIR analysis was performed to investigate the role of OmcA and MtrC in bacterial adhesion to goethite at the molecular level. After introduction of bacteria, the intensities of the amide I and II bands increase rapidly (Fig. S3). Since amide II is insensitive to structural changes, the area of the amide II band is used as an indicator of the amount of bacterial adhesion (25). Consistent with the QCM-D data, the amide II peak area of the WT increases rapidly during the first 2 h of attachment (Fig. S4), and based on this corroborated behavior, the surface reaction between the bacteria and goethite is separated into two phases, an initial 2-h fast attachment and a subsequent longer-term adhesion.

The interaction of bacterial cell surface functional groups with goethite was further resolved via 2D-CoS analysis. In the first 2 h, the sequence of interaction for the WT is as follows (Fig. S5):  $\nu_s(\text{PO}_2^-)$  ( $1,087\text{ cm}^{-1}$ ),  $\nu(\text{C-OH/C-O-C/C-C})$  ( $1,053\text{ cm}^{-1}$ ),  $\nu(\text{P-OFe})$  ( $1,046\text{ cm}^{-1}$ ) > amide I ( $1,645\text{ cm}^{-1}$ ), amide II ( $1,543\text{ cm}^{-1}$ ) (Table S2). The analysis also resolves the degree of changes in intensity, which is as follows:  $\nu_s(\text{PO}_2^-)$  ( $1,087\text{ cm}^{-1}$ ) >  $\nu(\text{C-OH/C-O-C/C-C})$  ( $1,053\text{ cm}^{-1}$ ) > amide II ( $1,543\text{ cm}^{-1}$ ) > amide I ( $1,645\text{ cm}^{-1}$ ). These results indicate that P moieties that mainly originated from phospholipids, lipopolysaccharide, and extracellular DNA (eDNA) are involved in the initial attachment. The phosphate groups exhibited high affinity toward iron oxides through the formation of covalent bonds (26–29).  $\nu_s(\text{PO}_2^-)$  at  $1,087\text{ cm}^{-1}$  and  $\nu(\text{P-OFe})$  at  $1,046\text{ cm}^{-1}$  manifest the formation of inner-sphere monodentate Fe-phosphate/phosphonate surface complexes during initial attachment (27). In the longer-term attachment, the sequential order becomes the following:  $\nu(\text{C-OH/C-O-C/C-C})$  ( $1,076\text{ cm}^{-1}$ ) > amide II ( $1,546\text{ cm}^{-1}$ ) > amide I ( $1,645\text{ cm}^{-1}$ ) (Table S3). The intensity follows the sequence  $\nu(\text{C-OH/C-O-C/C-C})$  ( $1,076\text{ cm}^{-1}$ ) > amide II ( $1,546\text{ cm}^{-1}$ ) > amide I ( $1,645\text{ cm}^{-1}$ ) >  $\nu_s(\text{COO}^-)$  ( $1,398\text{ cm}^{-1}$ ). These results indicate that C moieties of polysaccharides and surface proteins dominate interfacial interactions during the longer-term attachment.

The deletion of outer membrane *c*-Cyts is found to trigger pronounced differences in the mechanisms of the surface interfacial reactions (Fig. 6 and 7; Fig. S6). In the first 2 h, the sequences of interaction for the mutants lacking MtrC ( $\Delta\text{mtrC}$ ) and lacking both OmcA and MtrC ( $\Delta\text{omcA } \Delta\text{mtrC}$ ) are as follows:  $\nu_s(\text{PO}_2^-)$  ( $1,079\text{ cm}^{-1}$ ) >  $\nu_{\text{as}}(\text{PO}_2^-)$  ( $1,238\text{ cm}^{-1}$ ) > amide II ( $1,550\text{ cm}^{-1}$ ) > amide I ( $1,648\text{ cm}^{-1}$ ) (Table S4) and  $\nu(\text{C-OH/C-O-C/C-C})$  ( $1,051\text{ cm}^{-1}$ ),  $\nu_s(\text{PO}_2^-)$  ( $1,082\text{ cm}^{-1}$ ) >  $\nu_s(\text{COO}^-)$  ( $1,404\text{ cm}^{-1}$ ) > amide I ( $1,644\text{ cm}^{-1}$ ) > amide II ( $1,548\text{ cm}^{-1}$ ),  $\nu_{\text{as}}(\text{PO}_2^-)$  ( $1,236\text{ cm}^{-1}$ ) (Table S5), respectively. Meanwhile, the sequence of interaction for the mutant lacking OmcA ( $\Delta\text{omcA}$ ) is as follows:  $\delta(\text{CH}_3/\text{CH}_2)$  ( $1,462\text{ cm}^{-1}$ ) >  $\nu(\text{P-OFe})$  ( $1,046\text{ cm}^{-1}$ ),  $\nu_s(\text{PO}_2^-)$  ( $1,086\text{ cm}^{-1}$ ), amide II ( $1,548\text{ cm}^{-1}$ ) > amide I ( $1,646\text{ cm}^{-1}$ ) >  $\nu_s(\text{COO}^-)$  ( $1,400\text{ cm}^{-1}$ ) (Table S6). These results demonstrate that during the initial attachment stage, the WT and  $\Delta\text{mtrC}$  mutant attach to the goethite surface via P moieties  $\nu_s(\text{PO}_2^-)$  (Fig. 6 and S5), while the WT and the  $\Delta\text{omcA}$  mutant form inner-sphere monodentate Fe-phosphate/phosphonate surface complexes,  $\nu(\text{P-OFe})$  ( $1,046\text{ cm}^{-1}$ ) (Fig. 7 and S5), which are absent in the  $\Delta\text{mtrC}$  (Fig. 6) and  $\Delta\text{omcA } \Delta\text{mtrC}$  (Fig. S6) mutants. The longer-term attachment process for the  $\Delta\text{omcA}$  mutant (Table S7) is also analogous to that of the WT, in which C moieties of polysaccharides and surface proteins dominate the surface reactions. In the longer-term attachment process for the  $\Delta\text{mtrC}$  (Table S8) and  $\Delta\text{omcA } \Delta\text{mtrC}$  (Table S9) mutants, both polysaccharides and proteins are involved but also the phosphate groups contribute to the binding via formation of monodentate bonds [ $\nu_s(\text{PO}_2^-)$  ( $1,085\text{ cm}^{-1}$ ),  $\nu_{\text{as}}(\text{PO}_2^-)$  ( $1,226\text{ cm}^{-1}$ )]. Overall, these results suggest that MtrC contributes to the initial interfacial reaction between *S. oneidensis* MR-1 and goethite via an inner-sphere coordination between cell surface phosphate groups and the goethite surface.

**AFM analysis of the mechanical features of *S. oneidensis* MR-1 adhesion to goethite.** Colloidal probe AFM was used to investigate the interaction force between *S. oneidensis* strains and goethite. The largest adhesion force was observed for the WT

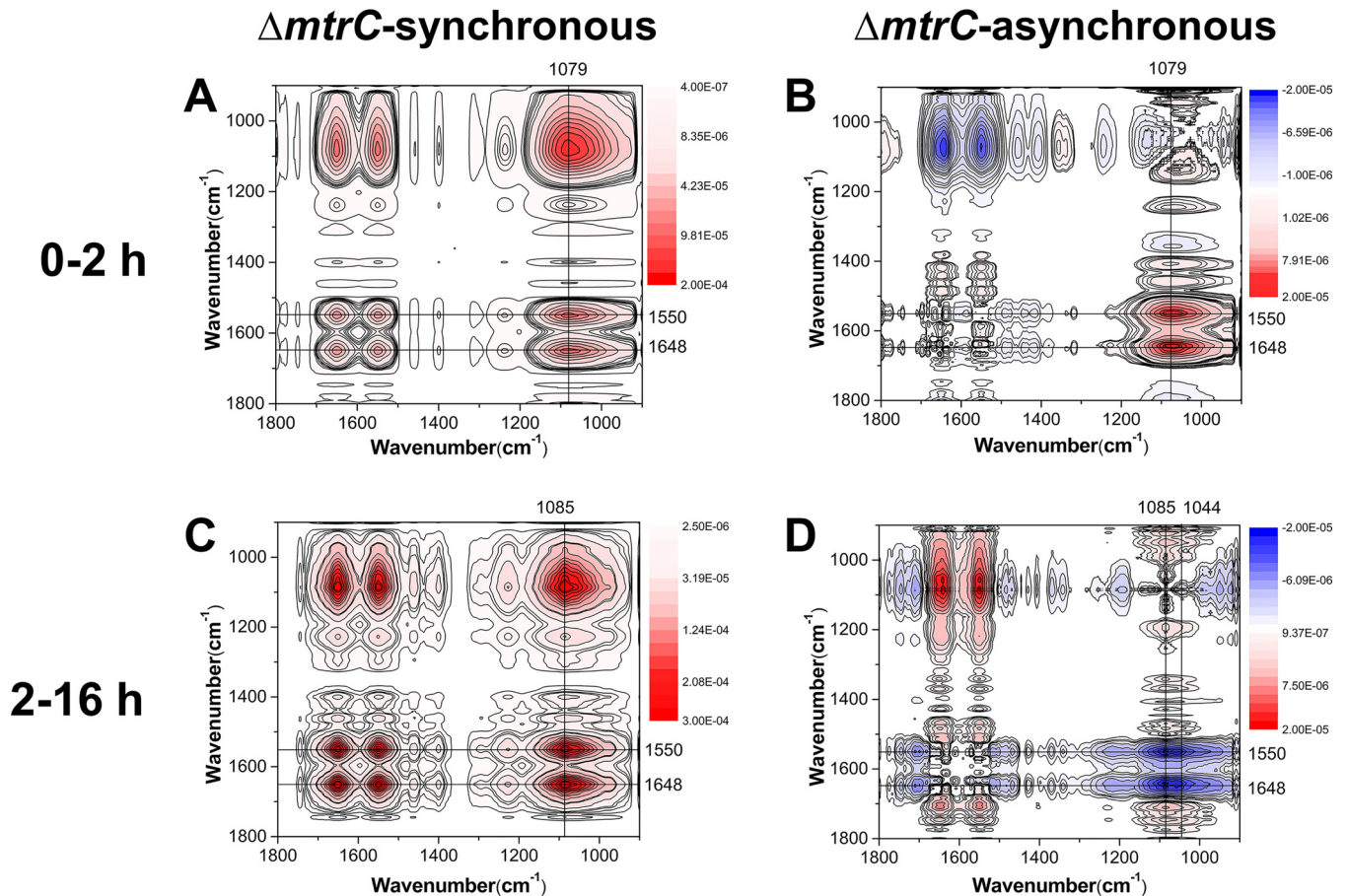


**FIG 6** Synchronous (A, C) and asynchronous (B, D) 2D correlation map of time-dependent ATR-FTIR spectra for the short-term (A, B) and long-term (C, D) attachment of  $\Delta mtrC$  cells to goethite. The red and blue regions represent positive and negative correlation intensities, respectively.

and the mutant lacking MtrC ( $\Delta mtrC$ ) upon retraction. The attractive force was  $1.17 \pm 0.05$  nN (mean  $\pm$  standard error,  $n = 100$ ) for the WT and  $1.18 \pm 0.05$  nN for the  $\Delta mtrC$  mutant (Fig. 8A and B). Meanwhile, when OmcA is lacking, the adhesion forces for the  $\Delta omcA$  and  $\Delta omcA \Delta mtrC$  strains are significantly reduced to  $0.71 \pm 0.03$  and  $0.75 \pm 0.03$  nN, respectively (Fig. 8C and D). The weak attraction force of the  $\Delta omcA$  and  $\Delta omcA \Delta mtrC$  mutants also corresponds to shorter rupture lengths (Table S10). The distance over which the attractive interaction between the WT and goethite occurs is more than twice that for the  $\Delta omcA \Delta mtrC$  mutant ( $P < 0.05$ ). The rupture length of the  $\Delta mtrC$  mutant is shorter than that of the WT but still significantly longer than that of mutants deficient in OmcA ( $P < 0.05$ ) (Table S10).

The sawtooth-like patterns in the retraction curves were analyzed to gain more definitive evidence for the role of OmcA and MtrC in the adhesion between *S. oneidensis* MR-1 and goethite. A single OmcA molecule composed of 748 amino acids corresponds to a contour length of 299 nm, while a single MtrC molecule composed of 692 amino acids has a contour length of 277 nm (15). Based on the prediction of the worm-like chain (WLC) model, the rupture events for the WT and  $\Delta mtrC$  mutant at about 291 nm (Fig. 8A) and 293 nm (Fig. 8B) are close to the contour length of OmcA, and 18% and 14% of the retraction curves ( $n = 100$ ) for the WT and  $\Delta mtrC$  mutant, respectively, exhibit the sawtooth-shaped force signature of OmcA. On the other hand, the frequencies of MtrC rupture events for the WT and  $\Delta omcA$  mutant are only 9% and 3%, respectively. Therefore, these results indicate that OmcA is central in the short-term interaction between *S. oneidensis* MR-1 and goethite, and its involvement in these interactions enhances the attractive force by about 60% (Table S10). This stronger



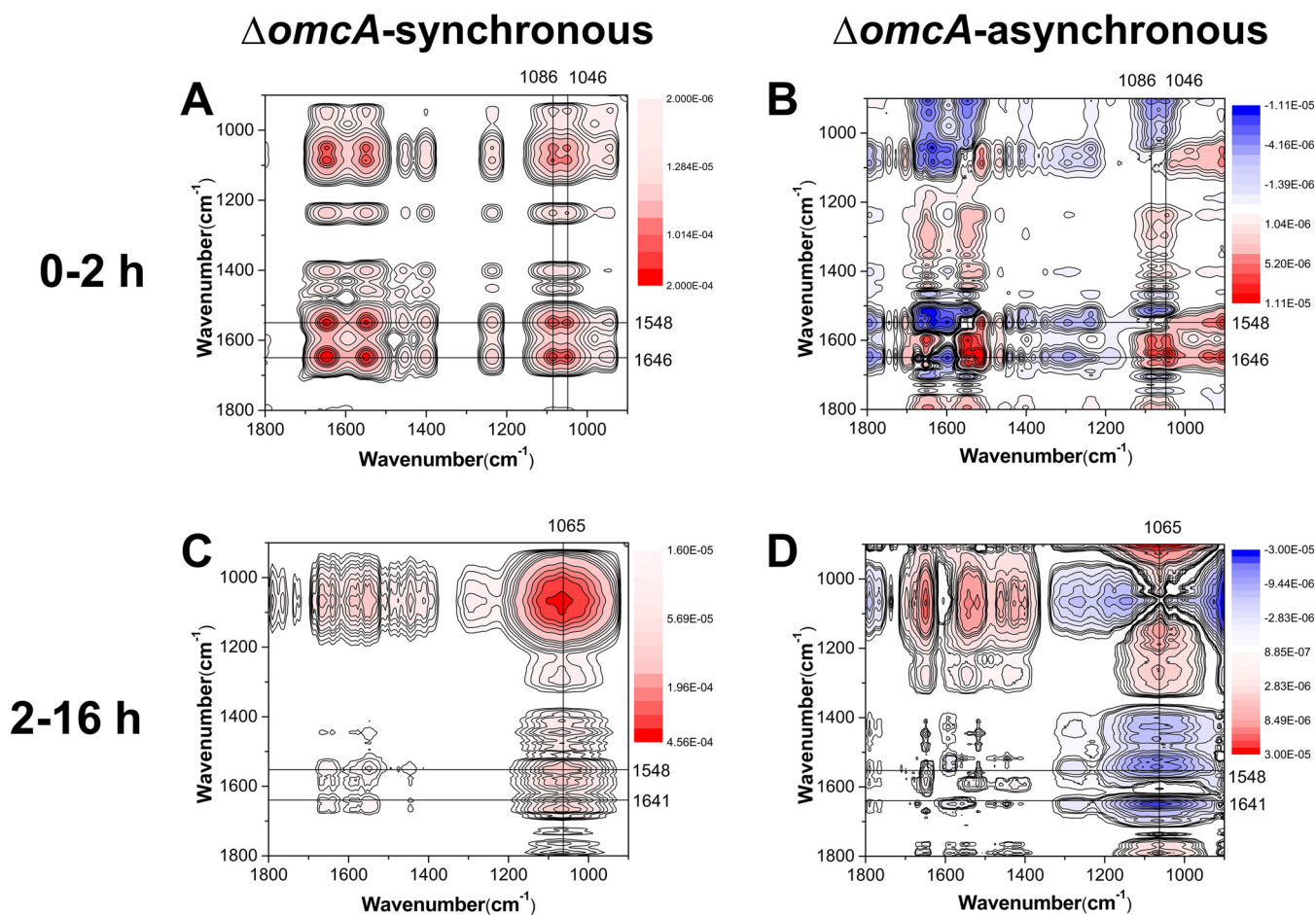


**FIG 7** Synchronous (A, C) and asynchronous (B, D) 2D correlation map of time-dependent ATR-FTIR spectra for the short-term (A, B) and long-term (C, D) attachment of  $\Delta omcA$  cells to goethite. The red and blue regions represent positive and negative correlation intensities, respectively.

binding force can induce more attachment, which correlates with more WT and  $\Delta mtrC$  cells attached to goethite in the initial attachment phase (Fig. 2).

## DISCUSSION

**Role of outer membrane c-Cyts in *S. oneidensis* attachment to goethite.** Based on the QCM-D dissipation shift ( $\Delta D$ ), there appear to be three stages of attachment to the goethite surface for the WT and mutants. All bacterial cells undergo a period of initial attachment, but this appears to be enhanced for the WT and the mutant lacking MtrC ( $\Delta mtrC$ ), compared to the mutant lacking OmcA ( $\Delta omcA$ ) and that lacking both OmcA and MtrC ( $\Delta omcA \Delta mtrC$ ). This result indicates that OmcA is important in the initial attachment phase. After this initial attachment, there appears to be a transition in the type and/or number of bacterial attachments for all the strains except the  $\Delta mtrC$  mutant, which shows a substantial increase in the amount of attached cells. This suggests that OmcA is somewhat less important than MtrC in the longer-term interactions of the cells with the goethite surfaces. In the third and final attachment phase, there appears to be a relatively stable assemblage of cells attached to the goethite surface.

To further elucidate the relative importance of OmcA and MtrC in the initial and subsequent stages of cell attachment, the viscoelastic properties of surface-associated cells can be evaluated via the slope of  $\Delta D$ - $\Delta f$  plots (21, 23). A flat slope indicates a rigid mass attachment (23). In the final attachment stage, the WT displays overlapping and flat slopes at overtones greater than 3 (Fig. S7). As the 3rd, 5th, 7th, and 9th overtones correspond to sensing depths of  $\sim 144$ , 110, 94, and 83 nm (23), respectively, the

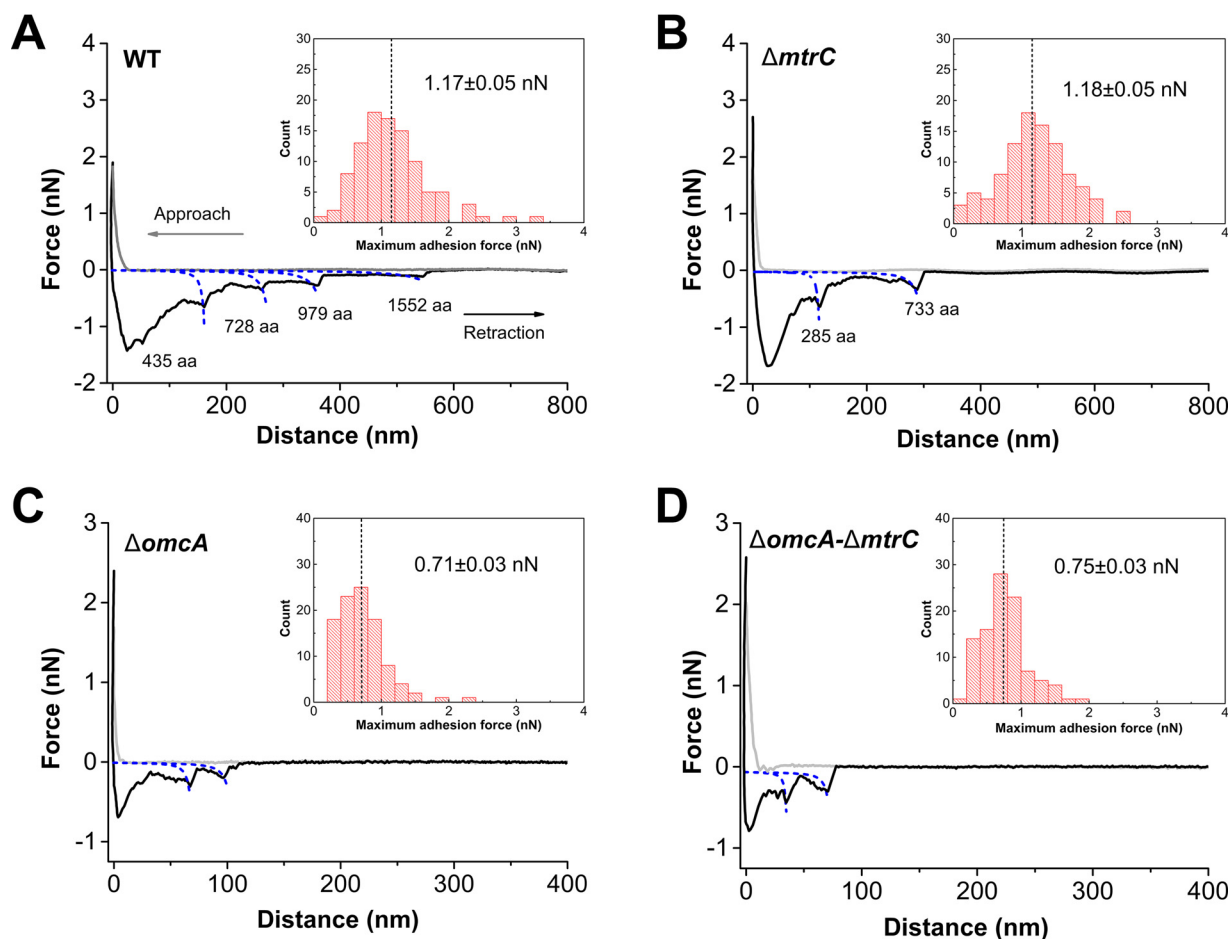


**FIG 8** Representative force-distance curves between the WT (A) and  $\Delta mtrC$  (B),  $\Delta omcA$  (C), and  $\Delta omcA \Delta mtrC$  (D) mutant strains and goethite under anaerobic conditions. Insets show the adhesion force distribution of 100 measurements.

overlapping slopes suggest that the WT forms a rigid bacterial layer with a thickness of about 110 nm. Consistent with the higher elastic constant, the slope of the  $\Delta omcA$  mutant is flatter than that of the  $\Delta mtrC$  mutant, which indicates higher rigidity of the attached bacteria (Fig. S7). As such, while OmcA is important in the initial stages of attachment, MtrC may be effective in developing longer-term stable bonds with goethite, which increase the rigidity of the attached bacteria and reduce the energy dissipation ( $\Delta D$ ).

**OmcA promotes rapid and strong bacterial adhesion to goethite.** Previous AFM studies have demonstrated that purified OmcA and MtrC form strong bonds with iron (hydr)oxide but that the binding strength of OmcA with iron (hydr)oxides is about twice that of MtrC (15, 17). Studies using single whole cells also reveal an absence of an MtrC unfolding trajectory during *Shewanella*-goethite interactions (30). Using multiple whole cells, the study here shows that during the initial attachment phase, the mutant lacking MtrC ( $\Delta mtrC$ ), and thus possessing OmcA, experiences considerable bacterial attachment and high cell densities at the goethite surface, comparable to the WT (Fig. 1 and 2). At the beginning of the second attachment stage, however, all the bacterial strains except the  $\Delta mtrC$  mutant show a substantial increase in bacterial attachment, suggesting that while OmcA is important for initial attachment, it is somewhat less important for driving subsequent longer-term attachment (Fig. 2). During the initial attachment phase, the  $\Delta mtrC$  mutant also experiences the largest adhesion force between the bacteria and goethite surfaces, again comparable to the WT (Fig. 8). The ATR-FTIR and 2D-CoS analyses suggest that  $\nu_5(\text{PO}_2^-)$  P moieties are primarily involved in the initial

attachment of both the WT and  $\Delta mtrC$  mutant (see Fig. 6 and S5 in the supplemental material). Taken together, these results indicate that the binding strength of OmcA is greater than that of MtrC during the initial attachment phase, which leads to a rapid and strong attachment of *S. oneidensis* MR-1 to the goethite surface, with MtrC contributing less to this short-term interaction. It should be noted that the AFM adhesion force measured in this study is slightly greater than that between single MR-1 cells and goethite (0.75 nN) (30). The difference may be ascribed to the binding of multiple cells with the goethite surface.

**MtrC promotes longer-term bacterial adhesion to goethite via microbial P moieties.** Following the initial attachment phase, at the beginning of the second attachment phase, this study shows that all the bacterial strains except the mutant lacking MtrC ( $\Delta mtrC$ ) show a substantial increase in bacterial attachment (Fig. 2). Furthermore, the presence of MtrC is shown to enhance the contact area between *S. oneidensis* MR-1 and goethite, where a higher contact area results in greater elastic and damping effects during the cell-mineral interaction (Table 1). The differential effects of OmcA and MtrC may be associated with their different orientations on cell surfaces. OmcA and MtrC contain similar structure and heme arrangements and can bind to iron oxides through their solvent-exposed hemes (4, 12). Since one of the solvent-exposed termini in MtrC was associated with periplasmic MtrA through transmembrane porin MtrB, MtrC was uniformly anchored and extended from the outer membrane surface (31–33). Meanwhile, the proper localization of OmcA on the cell surface is assisted by MtrC, without which OmcA attaches to the outer membrane merely via the N-terminal lipoprotein modification (34, 35). Therefore, OmcA in the  $\Delta mtrC$  mutant may move via lateral diffusion and stabilize at the *Shewanella*-goethite interface. The immunolocalization assay also demonstrates that the lack of MtrC causes a significant reduction in the coverage of *c*-Cyts on the cell surface (Fig. 5). This suggests that MtrC not only directly binds to goethite but also influences the interaction between OmcA and goethite.

The ATR-FTIR and 2D-CoS analyses suggest that the mutant lacking OmcA ( $\Delta omcA$ ), and thus possessing MtrC, interacts with the goethite surface via  $\nu(P-OFe)$  P moieties, forming inner-sphere monodentate Fe-phosphate/phosphonate surface complexes (Fig. 7). As such, it appears that after the initial attachment stage, MtrC promotes the attachment of *S. oneidensis* MR-1 to goethite via the formation of Fe-phosphate/phosphonate surface complexes. It should be noted that while  $\nu(P-OFe)$  P moieties are involved to some extent in the initial binding of both the WT and the mutant lacking OmcA ( $\Delta omcA$ ), and thus possessing MtrC, these do not provide the strongest adhesion during this first attachment step (Fig. 8C).

Overall, based on *in situ* ATR-FTIR 2D-CoS analysis, the attachment process for both the WT and mutants during the initial [ $\nu_s(PO_2^-)$ ] and subsequent [ $\nu(P-OFe)$ ] attachment phases is initiated by phosphate-bearing groups at the bacterial cell surface. The affinity of bacterial P moieties for iron (hydr)oxides are recognized for *S. putrefaciens*, *Pseudomonas aeruginosa*, and *Bacillus subtilis* (26, 27). Interestingly, recent work characterizes the surface reaction between *Shewanella* and iron (hydr)oxide under aerobic conditions (25, 27), and AFM analyses in particular demonstrate that the affinity between *Shewanella* and iron (hydr)oxides is significantly reduced under aerobic but not anaerobic conditions (11, 30, 36). A possible explanation for the reduced affinity between the bacteria and the mineral surface under aerobic conditions might lie in the fact that the attachment process of the WT under aerobic conditions is similar to those of the  $\Delta mtrC$  and  $\Delta omcA \Delta mtrC$  mutants under the anaerobic conditions of this study, in which phosphate groups react with goethite to play a central role in bacterial adhesion (25). Previous studies demonstrated that when *Shewanella* cells are exposed to oxygen, *c*-Cyts become embedded in the outer cell membrane (30, 37), such that their role in promoting initial attachment and longer-term binding via the phosphate groups is significantly reduced. Overall, it appears that different binding affinities and interfacial reactions between bacteria and goethite under aerobic and anaerobic conditions might be attributed mainly to the specific roles of outer membrane *c*-Cyts.

**Environmental significance.** Microbial dissimilatory iron reduction (DIR) is a fundamentally important process in subsurface soils and sediments, where it mediates the biogeochemical cycling of iron and carbon but also impacts the reactivity and cycling of other essential bioelements and contaminants through control of subsurface redox conditions (4). OmcA and MtrC are the terminal reductases on *Shewanella* cell surfaces that transfer electrons directly to solid minerals, which in turn drives DIR (1). Although the amounts of OmcA and MtrC at the cell surface and their molecular structures are largely comparable, previous studies have shown that MtrC rather than OmcA plays a more central role in DIR (8, 19, 20). This study investigates the role of *c*-Cyts in whole-cell interactions with the ubiquitous iron (hydr)oxide goethite. The results show that OmcA contributes to the initial attachment via a strong binding force and that MtrC enhances the contact area between bacteria and the goethite surface. As the high-contact area is associated with effective extracellular electron transfer (38–40), this study sheds new light on the indispensable function of MtrC in DIR. Overall, this study shows that besides transferring electrons, *c*-Cyts enhance the attachment of *Shewanella* cells to iron (hydr)oxides via two different strategies, specific to either OmcA in the initial attachment stage or to MtrC in the subsequent attachment stage. This rapid attachment and colonization of bacteria on iron (hydr)oxide minerals promoted by outer membrane *c*-type cytochromes confers to these strains a survival advantage in subsurface soils and sediments.

**Conclusions.** The outer membrane *c*-type cytochromes OmcA and MtrC are key terminal reductases for *Shewanella* cells to mediate extracellular electron transfer. Although previous studies on purified *c*-Cyts have revealed their similar structural properties, little is known about their roles in *Shewanella* bacterium-mineral interaction at the whole-cell level. This study demonstrates that OmcA and MtrC play distinct roles in *S. oneidensis* MR-1 attachment to goethite. OmcA contributes to a 60% greater attractive force between bacterial cells and the goethite surface and induces a rapid short-term attachment. Meanwhile, MtrC enhances the contact area of the bacterial cells with goethite by more than 2-fold and promotes the interfacial reaction and inner-sphere coordination between bacterial phosphate groups and the mineral surface. The increased contact area offered by MtrC may explain its central role in extracellular electron transfer.

## MATERIALS AND METHODS

**Bacteria and cultivation media.** Wild-type *S. oneidensis* MR-1 (WT) and three mutant strains ( $\Delta$ omcA,  $\Delta$ mtrC, and  $\Delta$ mtrC  $\Delta$ omcA mutants) have been described in previous studies (41). The phenotypes and genotypes of mutant strains were validated via PCR and immunolocalization (see Fig. S8 and S9 in the supplemental material). The cells were precultivated in Luria-Bertani (LB) medium under aerobic conditions at 30°C. After overnight cultivation, the cells were washed three times and resuspended in 0.1 M NaCl solution to a concentration of  $1 \times 10^8$  cells ml<sup>-1</sup>.

**Synthesis and characterization of goethite.** Goethite was synthesized by following previously reported approaches (42, 43). Briefly, 0.15 M Fe(NO<sub>3</sub>)<sub>3</sub> was added to 2.5 M KOH neutralizing solution. After aging for 24 h at 60°C, the mineralogy and morphology of the synthetic goethite were verified by X-ray diffraction (XRD) and transmission electron microscopy (TEM) analyses (Fig. S10). The average size of the goethite particles is  $195.8 \pm 42.9$  nm.

**QCM-D analysis of bacterial attachment to goethite.** The adhesion process was examined by using a QCM-D system (Q-Sense, Sweden). To begin with, a thin layer of goethite was spin-coated on a gold-plated sensor. The attachment processes of the WT and mutants on the bare gold sensor show no significant difference (Fig. S11). Cell-free 0.1 M NaCl solution at pH 7.0 was then injected for 4 h to establish a background signal. The bacterial solution (pH 7.0) was then introduced at a flow rate of 85  $\mu$ l/min. Based on on-line pH measurement, the pH of the bacterial suspension was kept constant at 7.0 by adding a dilute HCl or NaOH solution. The changes in oscillating frequency ( $\Delta f$ , Hz) and energy dissipation ( $\Delta D$ ) were recorded at five different overtones ( $n = 3, 5, 7, 9, \text{ and } 11$ ). During the measurement, the bacterial suspension was purged with nitrogen gas to ensure anaerobic conditions. Due to the absence of electron donors, goethite was not reduced during the bacterial attachment processes (Table S11). The cell viability was examined using a Live/Dead BacLight bacterial viability kit (catalog no. L7012) (44). More than 98% of cells were alive after incubation in 0.1 M NaCl for 11 h (Fig. S12). Bacteria that adhered to the QCM-D sensor were stained with SYTO 9 and observed under a confocal laser scanning microscope (FV1000; Olympus, Japan). Five images for each strain were collected, and the cell density was determined using IMARIS software (45).

**Modeling of QCM data.** A quantitative model of the QCM-D response was used to quantify the different interaction processes of *S. oneidensis* MR-1 with goethite at 10 h. The  $\Delta f_n$  and  $\Delta D_n$  values



obtained were fitted to the model to determine contact elasticity ( $\kappa_c$ ), contact damping ( $\xi_c$ ), and density of attached bacteria ( $N_p$ ) (24). After bacteria attach to the QCM-D surface, the load impedance is changed by  $\Delta Z_L^*$  and the complex frequency shift is given as  $\Delta f^* = \Delta f + i\Delta\Gamma$ . The frequency ( $\Delta f_n$ ) and bandwidth shifts ( $\Delta\Gamma_n$ ) at overtones  $n$  correspond to

$$\Delta f_n = -\frac{f_F}{\pi Z_q} \text{Im}(\Delta Z_L^*) \tag{1}$$

$$\Delta\Gamma_n = \frac{f_F n}{2} \Delta D_n = \frac{f_F}{\pi Z_q} \text{Re}(\Delta Z_L^*) \tag{2}$$

where  $f_F$  is the fundamental frequency which equals 5 MHz,  $\Delta D_n$  is the dissipation shift at overtone  $n$ , and  $Z_q$  is the acoustic impedance of an AT-cut quartz crystal [ $8.8 \times 10^6 \text{ kg}/(\text{m}^2\cdot\text{s})$ ].  $\text{Im}$  and  $\text{Re}$  are the imaginary part and real part, respectively, of the complex number  $Z_L^*$ .

The proposed equivalent circuit considered that the total  $\Delta f_{\text{total}}^*$  is determined by the sum of the reciprocals of the contact region and oscillating particle loads (Fig. 4):

$$\Delta f_{\text{total}}^* = \left( \frac{1}{\Delta f_p^*} + \frac{1}{\Delta f_c^*} \right)^{-1} \tag{3}$$

where  $\Delta f_p^*$  and  $\Delta f_c^*$  are the frequency shifts for an oscillating particle and the contact region, respectively.  $\Delta f_p^*$  can be obtained as:

$$\Delta f_p^* = \Delta f_p + i\Delta\Gamma_p = \frac{N_p}{Z_q} \left[ -\frac{8}{3}\pi R^3 \left( \rho_p + \frac{\rho}{2} \right) f_F^2 n + i6\pi^{0.5} R^2 (\eta\rho)^{0.5} f_F^{1.5} n^{0.5} \right] \tag{4}$$

where  $\rho$  and  $\eta$  are the liquid density and viscosity [ $0.009 \text{ g}/(\text{cm}\cdot\text{s})$ ], respectively,  $R$  is the radius of bacteria ( $1 \mu\text{m}$ ), and  $\rho_p$  is the bacterial density ( $1.348 \text{ g}/\text{cm}^3$ ) (24, 46).

The shift for contact region  $\Delta f_c^*$  is given as:

$$\Delta f_c^* = \Delta f_c + i\Delta\Gamma_c = N_p \frac{1}{1 - \eta_r/\eta_t} \left[ \frac{1}{2\pi^2 Z_q} \kappa_c n^{-1} + i \frac{f_F}{\pi Z_q} \xi_c n^0 \right] \tag{5}$$

where  $\eta_t$  and  $\eta_r$  are the resistance coefficients for particle translation and rotation, respectively:

$$\eta_t = i\frac{4}{3}\pi R^3 \left( \rho_p + \frac{\rho}{2} \right) \omega + 3\pi R^2 \rho \delta \omega \tag{6}$$

$$\eta_r = i\frac{8}{15}\pi R^3 \rho_p \omega + \frac{4}{3}\pi R^2 \rho \delta \omega \tag{7}$$

$\omega$  is the angular oscillation frequency, which equals  $2\pi n f_F$ ;  $\delta$  is the penetration depth:

$$\delta = \left( \frac{\eta}{\pi \rho f_F} \right)^{0.5} n^{-0.5} \tag{8}$$

Nonlinear regression was performed to minimize the deviation ( $d$ ) between experimental data ( $\Delta f_i^{\text{exp}}$  and  $\Delta\Gamma_i^{\text{exp}}$ ) and predicted values:

$$d = \sqrt{\sum_i (\Delta f_i^{\text{exp}} - \Delta f_i^{\text{model}})^2} + \sqrt{\sum_i (\Delta\Gamma_i^{\text{exp}} - \Delta\Gamma_i^{\text{model}})^2} \tag{9}$$

Monte Carlo simulation was used to construct the 95% confidence intervals (47).

The radius of the contact region,  $r_c$ , can be derived from the fitted  $\kappa_c$ :

$$r_c = \left( \frac{3\kappa_c R^2}{4E_c} \right)^{1/3} \tag{10}$$

where  $E_c$  is the Young's modulus of the bacterium-substrate interface:

$$E_c = \left( \frac{1 - \nu_p}{E_p} + \frac{1 - \nu_s}{E_s} \right)^{-1} \tag{11}$$

and where  $\nu_p$  and  $E_p$  are the Poisson ratio and Young's modulus of *S. oneidensis* MR-1, which are taken as 0.5 and 100 MPa, respectively (48).  $\nu_s$  and  $E_s$  for goethite equal 0.22 and 358 GPa, respectively (49).

**Immunolocalization of c-Cyts on cell surface.** The distribution of OmcA and MtrC was revealed by an immunolocalization assay. Affinity-purified antibodies toward the hydrophilic and surface-exposed regions of MtrC and OmcA were prepared based on a previous study (see supplemental material for details) (41). *Shewanella* cells ( $4.8 \times 10^7$  cells/ml) were incubated with goethite (0.02 g/liter) in 0.1 M NaCl solution anaerobically for 11 h. The culture was then fixed in 4% paraformaldehyde for 15 min and washed with phosphate-buffered saline (PBS). Goethite was dissolved by oxalic acid (15 g/liter, pH 3.0) (50). After blocking in 1% bovine serum albumin (BSA) solution, the samples were subjected to reaction with the primary antibody and secondary anti-rabbit Alexa488 antibody sequentially. Cells were counterstained with 4',6-diamidino-2-phenylindole (DAPI) and observed using structured illumination microscopy (SIM; Nikon). Manders' overlap coefficient (MOC) was calculated to describe the coverage of c-Cyts on the cell surface in which a higher MOC suggests higher coverage (51). The MOC was calculated as follows:

$$R = \frac{\sum_i S1_i \cdot S2_i}{\sqrt{\sum_i (S1_i)^2 \cdot \sum_i (S2_i)^2}} \tag{12}$$

where  $S1_i$  represents the signal intensity of the  $i^{\text{th}}$  pixel in the blue channel and  $S2_i$  represents the signal intensity of the  $i^{\text{th}}$  pixel in the green channel.

**ATR-FTIR and 2D-CoS analysis.** A Fourier transform infrared (FTIR) spectrometer (Bruker IFS 66v/s) equipped with a liquid nitrogen-cooled detector was used for FTIR analysis. The spectra were recorded over the range of 400 to 4,000  $\text{cm}^{-1}$  with a resolution of 4  $\text{cm}^{-1}$ . *In situ* measurement of *S. oneidensis* MR-1 adhesion to the goethite surface was conducted in accordance with previous studies (25, 27). Briefly, the goethite suspension was spread on the crystal surface of a ZnSe ATR flow cell. After drying for 12 h at 37°C, a goethite film was formed on the ZnSe crystal. The cell-free 0.1 M NaCl solution was then injected into the flow cell to obtain a background spectrum. After 2 h, the bacterial suspension was pumped into the flow cell by a peristaltic pump at 1 ml/min. During the measurement, the bacterial suspension was purged with nitrogen gas to ensure anaerobic conditions and the pH was kept constant at 7.0 by adding a small amount of dilute HCl or NaOH. Spectra were recorded for 16 h until no further changes were observed. The ATR-FTIR spectra of the bacterium-goethite samples were obtained by subtracting the background spectrum.

The 2D correlation analysis of attached bacteria was performed by using 2DShige software (Shigeaki Morita, Japan) (25, 52, 53). In this analysis, contact time was used as the external perturbation for the interaction of outer membrane *c*-type cytochromes (OMCs) with goethite. The calculations were carried out by using Origin 8.5. An analytical spectrum  $U(\nu, t)$  is considered to illustrate how the technique works. The variable  $\nu$  is the index variable for the FTIR spectra caused by the perturbation variable  $t$ . A discrete set of dynamic spectra measured at  $m$  equally spaced points in time  $t$  between  $T_{\min}$  and  $T_{\max}$  can be expressed by the following equation:

$$U_j(\nu) = y(\nu, t_j), j = 1, 2, \dots, m \quad (13)$$

A set of dynamic spectra can be represented as follows:

$$\tilde{U}(\nu, t) = U(\nu, t) - \bar{U}(\nu) \quad (14)$$

where  $\bar{U}(\nu)$  represents the reference spectrum, which is the average spectrum and can be calculated as follows:

$$\bar{U}(\nu) = \frac{1}{m} \sum_{j=1}^m U(\nu, t_j) \quad (15)$$

The synchronous correlation intensity can be directly gained by the following equation:

$$\Phi(\nu_1, \nu_2) = \frac{1}{m-1} \sum_{j=1}^m \tilde{U}_j(\nu_1) \tilde{U}_j(\nu_2) \quad (16)$$

The asynchronous correlation intensity can be obtained as follows:

$$\Psi(\nu_1, \nu_2) = \frac{1}{m-1} \sum_{j=1}^m \tilde{U}_j(\nu_1) \sum_{k=1}^m M_{jk} \tilde{U}_j(\nu_2) \quad (17)$$

The term  $M_{jk}$  corresponds to the  $j^{\text{th}}$  column and the  $k^{\text{th}}$  row element of the discrete Hilbert-Noda transformation matrix, which can be calculated as follows:

$$M_{jk} = \begin{cases} 0 & \text{if } j = k \\ \frac{1}{\pi(k-j)} & \text{otherwise} \end{cases} \quad (18)$$

The intensity of a synchronous correlation spectrum  $\Phi(\nu_1, \nu_2)$  represents the simultaneous or coincidental changes of two separate spectral intensity variations measured at  $\nu_1$  and  $\nu_2$  during the interval between  $T_{\min}$  and  $T_{\max}$  of the externally defined variable  $t$ . The intensity of an asynchronous spectrum  $\Psi(\nu_1, \nu_2)$  represents sequential or successive, but not coincidental, changes of spectral intensities measured separately at  $\nu_1$  and  $\nu_2$ . The rank order of intensity change between two bands at  $\nu_1$  and  $\nu_2$  can be obtained from the signs of the synchronous correlation peak  $\Phi(\nu_1, \nu_2)$  and asynchronous correlation peak  $\Psi(\nu_1, \nu_2)$  based on previously established principles (53–55). Basically, the sign of the synchronous correlation peak  $\Phi(\nu_1, \nu_2)$  is positive when the spectral intensities of band  $\nu_1$  and band  $\nu_2$  are either increasing or decreasing together during the observation period ( $t$ ); otherwise, the sign is negative. For the asynchronous correlation peak  $\Psi(\nu_1, \nu_2)$ , the sign is positive when the change in the intensity of band  $\nu_1$  occurs prior to that of band  $\nu_2$ ; otherwise, the sign is negative. When  $\Phi(\nu_1, \nu_2)$  and  $\Psi(\nu_1, \nu_2)$  have the same signs, the intensity change of band  $\nu_1$  occurs predominantly before that of band  $\nu_2$ ; when they have the opposite signs, the change order is reverse. The changes of band  $\nu_1$  and band  $\nu_2$  occur simultaneously when  $\Psi(\nu_1, \nu_2)$  equals zero (53–55).

As the changes in spectral intensity represent the interaction of the corresponding IR bands and outer membrane *c*-Cyt functional groups, the order in which the spectral intensity changes reflects the sequence in which the IR bands and the corresponding outer membrane *c*-Cyt functional groups interact with the goethite surface. In this way, the results obtained from 2D-CoS can reflect the order in which the different outer membrane *c*-Cyt functional groups interact and bind with goethite.

**AFM analysis of adhesion force.** Prior to adhesion of bacteria to the AFM cantilever, 6.1- $\mu\text{m}$ -radius silica beads (Bangs Laboratories) were rinsed with deionized water and dried on a glass slide. The beads were mounted onto a triangular tipless AFM cantilever (Bruker) coated with UV-curable glue (adhesive 63; Norland Products) (56). After 30 min of UV exposure, the colloidal probe was washed with ethanol and deionized water. The rinsed probe was immersed into 0.01% poly-L-lysine (Sigma) solution for 1 min to yield a positively charged surface. The cantilever was then dipped into the bacterial suspension ( $1 \times 10^{10}$  cells/ml) for 1 min to immobilize the bacteria on the silica beads. The goethite substratum was prepared as previously described (57). Briefly, 0.4 ml of goethite suspension (1 g/liter) was pipetted onto

a glass slide and then dried at 120°C. After rinsing in deionized water, the goethite-coated slide was sterilized by autoclaving. The force measurement was conducted using a MultiMode 8 AFM system with a NanoScope V controller (Bruker). The mechanical data were obtained in the contact mode in an N<sub>2</sub>-purged 0.1 M NaCl solution at a scan rate of 1 Hz. The ramp size was 1 μm, and the trigger threshold was 2 nN. A contact time of 10 s was used. The worm-like chain (WLC) model was used to estimate the retraction curve for bacterial surface biopolymers. The theoretical force-extension  $F(D)$  relationship is given as:

$$F(D) = \left( \frac{k_B T}{p} \right) \cdot \left[ 0.25 \left( 1 - \frac{D}{L} \right)^{-2} + \frac{D}{L} - 0.25 \right] \quad (19)$$

where  $D$  is the extension,  $k_B$  is the Boltzmann constant ( $1.38 \times 10^{-23}$  J/K),  $T$  is the temperature (in K),  $p$  is the persistence length, and  $L$  is the biopolymer's contour length (58).

**Statistics.** All attachment experiments were performed in triplicate. Statistical analysis was performed by using Student's  $t$  test. A  $P$  value higher than 0.05 indicates no significant difference within the 95% confidence interval.

## SUPPLEMENTAL MATERIAL

Supplemental material is available online only.

**SUPPLEMENTAL FILE 1**, PDF file, 1.7 MB.

## ACKNOWLEDGMENTS

This work was supported by the National Natural Science Foundation of China (grant no. 41807024), the National Basic Research Program of China (grant no. 2016YFD0800206), the Fundamental Research Funds for the Central Universities (program no. 52902-0900201674), and a Royal Society Newton Advance Fellowship (no. NAF/R1/191017).

We declare no competing financial interests.

## REFERENCES

- Lovley DR. 1991. Dissimilatory Fe(III) and Mn(IV) reduction. *Microbiol Mol Biol Rev* 55:259–287. <https://doi.org/10.1128/MMBR.55.2.259-287.1991>.
- Schwertmann U. 1993. Relations between iron oxides, soil color, and soil formation. *Soil Color* 31:51–69.
- Ponnamperuma FN. 1972. The chemistry of submerged soils, p 29–96. *In* Advances in agronomy, vol 24. Academic Press, New York, NY.
- Shi L, Dong H, Reguera G, Beyenal H, Lu A, Liu J, Yu HQ, Fredrickson JK. 2016. Extracellular electron transfer mechanisms between microorganisms and minerals. *Nat Rev Microbiol* 14:651–662. <https://doi.org/10.1038/nrmicro.2016.93>.
- Fredrickson JK, Romine MF, Beliaev AS, Auchtung JM, Driscoll ME, Gardner TS, Nealon KH, Osterman AL, Pinchuk G, Reed JL, Rodionov DA, Rodrigues JL, Saffarini DA, Serres MH, Spormann AM, Zhulin IB, Tiedje JM. 2008. Towards environmental systems biology of *Shewanella*. *Nat Rev Microbiol* 6:592–603. <https://doi.org/10.1038/nrmicro1947>.
- Shi L, Rosso KM, Clarke TA, Richardson DJ, Zachara JM, Fredrickson JK. 2012. Molecular underpinnings of Fe(III) oxide reduction by *Shewanella Oneidensis* MR-1. *Front Microbiol* 3:50. <https://doi.org/10.3389/fmicb.2012.00050>.
- Mitchell AC, Peterson L, Reardon CL, Reed SB, Culley DE, Romine MR, Geesey GG. 2012. Role of outer membrane c-type cytochromes MtrC and OmcA in *Shewanella oneidensis* MR-1 cell production, accumulation, and detachment during respiration on hematite. *Geobiology* 10:355–370. <https://doi.org/10.1111/j.1472-4669.2012.00321.x>.
- Bretschger O, Obratsova A, Sturm CA, Chang IS, Gorby YA, Reed SB, Culley DE, Reardon CL, Barua S, Romine MF, Zhou J, Beliaev AS, Bouhenni R, Saffarini D, Mansfeld F, Kim BH, Fredrickson JK, Nealon KH. 2007. Current production and metal oxide reduction by *Shewanella oneidensis* MR-1 wild type and mutants. *Appl Environ Microbiol* 73:7003–7012. <https://doi.org/10.1128/AEM.01087-07>.
- Ross DE, Brantley SL, Tien M. 2009. Kinetic characterization of OmcA and MtrC, terminal reductases involved in respiratory electron transfer for dissimilatory iron reduction in *Shewanella oneidensis* MR-1. *Appl Environ Microbiol* 75:5218–5226. <https://doi.org/10.1128/AEM.00544-09>.
- Borloo J, Vergauwen B, De Smet L, Brige A, Motte B, Devreese B, Van Beeumen J. 2007. A kinetic approach to the dependence of dissimilatory metal reduction by *Shewanella oneidensis* MR-1 on the outer membrane cytochromes c OmcA and OmcB. *FEBS J* 274:3728–3738. <https://doi.org/10.1111/j.1742-4658.2007.05907.x>.
- Lower BH, Yongsunthorn R, Shi L, Wildling L, Gruber HJ, Wigginton NS, Reardon CL, Pinchuk GE, Droubay TC, Boily JF, Lower SK. 2009. Antibody recognition force microscopy shows that outer membrane cytochromes OmcA and MtrC are expressed on the exterior surface of *Shewanella oneidensis* MR-1. *Appl Environ Microbiol* 75:2931–2935. <https://doi.org/10.1128/AEM.02108-08>.
- Shi L, Richardson DJ, Wang Z, Kerisit SN, Rosso KM, Zachara JM, Fredrickson JK. 2009. The roles of outer membrane cytochromes of *Shewanella* and *Geobacter* in extracellular electron transfer. *Environ Microbiol Rep* 1:220–227. <https://doi.org/10.1111/j.1758-2229.2009.00035.x>.
- Lower BH, Lins RD, Oestreicher Z, Straatsma TP, Hochella MF, Shi LA, Lower SK. 2008. In vitro evolution of a peptide with a hematite binding motif that may constitute a natural metal-oxide binding archetype. *Environ Sci Technol* 42:3821–3827. <https://doi.org/10.1021/es702688c>.
- Edwards MJ, Baiden NA, Johs A, Tomanicek SJ, Liang L, Shi L, Fredrickson JK, Zachara JM, Gates AJ, Butt JN, Richardson DJ, Clarke TA. 2014. The X-ray crystal structure of *Shewanella oneidensis* OmcA reveals new insight at the microbe-mineral interface. *FEBS Lett* 588:1886–1890. <https://doi.org/10.1016/j.febslet.2014.04.013>.
- Lower BH, Shi L, Yongsunthorn R, Droubay TC, McCready DE, Lower SK. 2007. Specific bonds between an iron oxide surface and outer membrane cytochromes MtrC and OmcA from *Shewanella oneidensis* MR-1. *J Bacteriol* 189:4944–4952. <https://doi.org/10.1128/JB.01518-06>.
- Sheng A, Liu F, Shi L, Liu J. 2016. Aggregation kinetics of hematite particles in the presence of outer membrane cytochrome OmcA of *Shewanella oneidensis* MR-1. *Environ Sci Technol* 50:11016–11024. <https://doi.org/10.1021/acs.est.6b02963>.
- Xiong Y, Shi L, Chen B, Mayer MU, Lower BH, Londer Y, Bose S, Hochella MF, Fredrickson JK, Squier TC. 2006. High-affinity binding and direct electron transfer to solid metals by the *Shewanella oneidensis* MR-1 outer membrane c-type cytochrome OmcA. *J Am Chem Soc* 128:13978–13979. <https://doi.org/10.1021/ja063526d>.
- Liu J, Pearce CI, Shi L, Wang Z, Shi Z, Arenholz E, Rosso KM. 2016. Particle size effect and the mechanism of hematite reduction by the outer membrane cytochrome OmcA of *Shewanella oneidensis* MR-1. *Geochim Cosmochim Acta* 193:160–175. <https://doi.org/10.1016/j.gca.2016.08.022>.
- Myers JM, Myers CR. 2001. Role for outer membrane cytochromes OmcA and OmcB of *Shewanella putrefaciens* MR-1 in reduction of manganese

- dioxide. *Appl Environ Microbiol* 67:260–269. <https://doi.org/10.1128/AEM.67.1.260-269.2001>.
20. Coursolle D, Gralnick JA. 2010. Modularity of the Mtr respiratory pathway of *Shewanella oneidensis* strain MR-1. *Mol Microbiol* 77:995–1008. <https://doi.org/10.1111/j.1365-2958.2010.07266.x>.
  21. Kao WL, Chang HY, Lin KY, Lee YW, Shyue JJ. 2018. Assessment of the effects of surface potential on the kinetics of HEK293T cell adhesion behavior using a quartz crystal microbalance with dissipation monitoring. *J Phys Chem C* 122:694–704. <https://doi.org/10.1021/acs.jpcc.7b11072>.
  22. Sadman K, Wiener CG, Weiss RA, White CC, Shull KR, Vogt BD. 2018. Quantitative rheometry of thin soft materials using the quartz crystal microbalance with dissipation. *Anal Chem* 90:4079–4088. <https://doi.org/10.1021/acs.analchem.7b05423>.
  23. Kao WL, Chang HY, Lin KY, Lee YW, Shyue JJ. 2017. Effect of surface potential on the adhesion behavior of NIH3T3 cells revealed by quartz crystal microbalance with dissipation monitoring (QCM-D). *J Phys Chem C* 121:533–541. <https://doi.org/10.1021/acs.jpcc.6b11217>.
  24. Tarnapolsky A, Freger V. 2018. Modeling QCM-D response to deposition and attachment of microparticles and living cells. *Anal Chem* 90:13960–13968. <https://doi.org/10.1021/acs.analchem.8b03411>.
  25. Yan W, Wang H, Jing C. 2016. Adhesion of *Shewanella oneidensis* MR-1 to goethite: a two-dimensional correlation spectroscopic study. *Environ Sci Technol* 50:4343–4349. <https://doi.org/10.1021/acs.est.6b00066>.
  26. Parikh SJ, Chorover J. 2006. ATR-FTIR spectroscopy reveals bond formation during bacterial adhesion to iron oxide. *Langmuir* 22:8492–8500. <https://doi.org/10.1021/la061359p>.
  27. Elzinga EJ, Huang JH, Chorover J, Kretschmar R. 2012. ATR-FTIR spectroscopy study of the influence of pH and contact time on the adhesion of *Shewanella putrefaciens* bacterial cells to the surface of hematite. *Environ Sci Technol* 46:12848–12855. <https://doi.org/10.1021/es303318y>.
  28. Omoike A, Chorover J, Kwon KD, Kubicki JD. 2004. Adhesion of bacterial exopolymers to  $\alpha$ -FeOOH: inner-sphere complexation of phosphodiester groups. *Langmuir* 20:11108–11114. <https://doi.org/10.1021/la048597+>.
  29. Jiang W, Saxena A, Song B, Ward BB, Beveridge TJ, Myneni SCB. 2004. Elucidation of functional groups on gram-positive and gram-negative bacterial surfaces using infrared spectroscopy. *Langmuir* 20:11433–11442. <https://doi.org/10.1021/la049043+>.
  30. Lower SK, Hochella MF, Beveridge TJ. 2001. Bacterial recognition of mineral surfaces: nanoscale interactions between *Shewanella* and  $\alpha$ -FeOOH. *Science* 292:1360–1363. <https://doi.org/10.1126/science.1059567>.
  31. Nakano CM, Byun HS, Ma H, Wei T, El-Naggar MY. 2015. A framework for stochastic simulations and visualization of biological electron-transfer dynamics. *Comput Phys Commun* 193:1–9. <https://doi.org/10.1016/j.cpc.2015.03.009>.
  32. Clarke TA, Edwards MJ, Gates AJ, Hall A, White GF, Bradley J, Reardon CL, Shi L, Beliaev AS, Marshall MJ, Wang Z, Watmough NJ, Fredrickson JK, Zachara JM, Butt JN, Richardson DJ. 2011. Structure of a bacterial cell surface decaheme electron conduit. *Proc Natl Acad Sci U S A* 108:9384–9389. <https://doi.org/10.1073/pnas.1017200108>.
  33. Edwards MJ, White GF, Lockwood CW, Lawes MC, Martel A, Harris G, Scott DJ, Richardson DJ, Butt JN, Clarke TA. 2018. Structural modeling of an outer membrane electron conduit from a metal-reducing bacterium suggests electron transfer via periplasmic redox partners. *J Biol Chem* 293:8103–8112. <https://doi.org/10.1074/jbc.RA118.001850>.
  34. Paquete CM, Fonseca BM, Cruz DR, Pereira TM, Pacheco I, Soares CM, Louro RO. 2014. Exploring the molecular mechanisms of electron shuttling across the microbe/metal space. *Front Microbiol* 5:318. <https://doi.org/10.3389/fmicb.2014.00318>.
  35. Johs A, Shi L, Droubay T, Ankner JF, Liang L. 2010. Characterization of the decaheme c-type cytochrome OmcA in solution and on hematite surfaces by small angle x-ray scattering and neutron reflectometry. *Biophys J* 98:3035–3043. <https://doi.org/10.1016/j.bpj.2010.03.049>.
  36. Roberts JA, Fowle DA, Hughes BT, Kulczycki E. 2006. Attachment behavior of *Shewanella putrefaciens* onto magnetite under aerobic and anaerobic conditions. *Geomicrobiol J* 23:631–640. <https://doi.org/10.1080/01490450600964441>.
  37. Sokolov I, Smith DS, Henderson GS, Gorby YA, Ferris FG. 2001. Cell surface electrochemical heterogeneity of the Fe(III)-reducing bacteria *Shewanella putrefaciens*. *Environ Sci Technol* 35:341–347. <https://doi.org/10.1021/es001258s>.
  38. Yan B, Wrenn BA, Basak S, Biswas P, Giammar DE. 2008. Microbial reduction of Fe(III) in hematite nanoparticles by *Geobacter sulfurreducens*. *Environ Sci Technol* 42:6526–6531. <https://doi.org/10.1021/es800620f>.
  39. Bose S, Hochella MF, Gorby YA, Kennedy DW, McCready DE, Madden AS, Lower BH. 2009. Bioreduction of hematite nanoparticles by the dissimilatory iron reducing bacterium *Shewanella oneidensis* MR-1. *Geochim Cosmochim Acta* 73:962–976. <https://doi.org/10.1016/j.gca.2008.11.031>.
  40. Roden EE, Zachara JM. 1996. Microbial reduction of crystalline iron(III) oxides: influence of oxide surface area and potential for cell growth. *Environ Sci Technol* 30:1618–1628. <https://doi.org/10.1021/es9506216>.
  41. Marshall MJ, Beliaev AS, Dohnalkova AC, Kennedy DW, Shi L, Wang Z, Boyanov MI, Lai B, Kemner KM, McLean JS, Reed SB, Culley DE, Bailey VL, Simonson CJ, Saffarini DA, Romine MF, Zachara JM, Fredrickson JK. 2006. c-type cytochrome-dependent formation of U(IV) nanoparticles by *Shewanella oneidensis*. *PLoS Biol* 4:e268. <https://doi.org/10.1371/journal.pbio.0040268>.
  42. Atkinson R, Posner A, Quirk JP. 1967. Adsorption of potential-determining ions at the ferric oxide-aqueous electrolyte interface. *J Phys Chem* 71:550–558. <https://doi.org/10.1021/j100862a014>.
  43. Lin D, Cai P, Peacock CL, Wu Y, Gao C, Peng W, Huang Q, Liang W. 2018. Towards a better understanding of the aggregation mechanisms of iron (hydr)oxide nanoparticles interacting with extracellular polymeric substances: role of pH and electrolyte solution. *Sci Total Environ* 645:372–379. <https://doi.org/10.1016/j.scitotenv.2018.07.136>.
  44. Wu Y, Mohanty A, Chia WS, Cao B. 2016. Influence of 3-chloroaniline on the biofilm lifestyle of *Comamonas testosteroni* and its implications on bioaugmentation. *Appl Environ Microbiol* 82:4401–4409. <https://doi.org/10.1128/AEM.00874-16>.
  45. Wu Y, Zaiden N, Liu X, Mukherjee M, Cao B. 2020. Responses of exogenous bacteria to soluble extracellular polymeric substances in wastewater: a mechanistic study and implications on bioaugmentation. *Environ Sci Technol* 54:6919–6928. <https://doi.org/10.1021/acs.est.0c00015>.
  46. Lewis K, Tzivilakis J, Green A, Warner D. 2013. Bio-pesticides database (BPDB). <http://sitem.herts.ac.uk/aeru/ppdb/en/index.htm>. Accessed 26 July 2019.
  47. Lambert RJW, Mytilinaios I, Maitland L, Brown AM. 2012. Monte Carlo simulation of parameter confidence intervals for non-linear regression analysis of biological data using Microsoft Excel. *Comput Methods Programs Biomed* 107:155–163. <https://doi.org/10.1016/j.cmpb.2011.05.009>.
  48. Tuson HH, Auer GK, Renner LD, Hasebe M, Terpini C, Salick M, Crone WC, Gopinathan A, Huang KC, Weibel DB. 2012. Measuring the stiffness of bacterial cells from growth rates in hydrogels of tunable elasticity. *Mol Microbiol* 84:874–891. <https://doi.org/10.1111/j.1365-2958.2012.08063.x>.
  49. Chicot D, Mendoza J, Zaoui A, Louis G, Lepingle V, Roudet F, Lesage J. 2011. Mechanical properties of magnetite (Fe<sub>3</sub>O<sub>4</sub>), hematite ( $\alpha$ -Fe<sub>2</sub>O<sub>3</sub>) and goethite ( $\alpha$ -FeO(OH)) by instrumented indentation and molecular dynamics analysis. *Mater Chem Phys* 129:862–870. <https://doi.org/10.1016/j.matchemphys.2011.05.056>.
  50. Reardon CL, Dohnalkova AC, Nachimuthu P, Kennedy DW, Saffarini DA, Arey BW, Shi L, Wang Z, Moore D, McLean JS, Moyles D, Marshall MJ, Zachara JM, Fredrickson JK, Beliaev AS. 2010. Role of outer-membrane cytochromes MtrC and OmcA in the biomineralization of ferrihydrite by *Shewanella oneidensis* MR-1. *Geobiology* 8:56–68. <https://doi.org/10.1111/j.1472-4669.2009.00226.x>.
  51. Zinchuk V, Zinchuk O, Okada T. 2007. Quantitative colocalization analysis of multicolor confocal immunofluorescence microscopy images: pushing pixels to explore biological phenomena. *Acta Histochem Cytochem* 40:101–111. <https://doi.org/10.1267/ahc.07002>.
  52. Schmidt MP, Martínez CE. 2016. Kinetic and conformational insights of protein adsorption onto montmorillonite revealed using in situ ATR-FTIR/2D-COS. *Langmuir* 32:7719–7729. <https://doi.org/10.1021/acs.langmuir.6b00786>.
  53. Cai P, Lin D, Peacock CL, Peng W, Huang Q. 2018. EPS adsorption to goethite: molecular level adsorption mechanisms using 2D correlation spectroscopy. *Chem Geol* 494:127–135. <https://doi.org/10.1016/j.chemgeo.2018.07.028>.
  54. Domínguez-Vidal A, Saenz-Navajas MP, Ayora-Cañada MJ, Lendl B. 2006. Detection of albumin unfolding preceding proteolysis using Fourier transform infrared spectroscopy and chemometric data analysis. *Anal Chem* 78:3257–3264. <https://doi.org/10.1021/ac0520137>.
  55. Jia Q, Wang N-N, Yu Z-W. 2009. An insight into sequential order in



- two-dimensional correlation spectroscopy. *Appl Spectrosc* 63: 344–353. <https://doi.org/10.1366/000370209787598861>.
56. Li X, Logan BE. 2004. Analysis of bacterial adhesion using a gradient force analysis method and colloid probe atomic force microscopy. *Langmuir* 20:8817–8822. <https://doi.org/10.1021/la0488203>.
57. Huang Q, Wu H, Cai P, Fein JB, Chen W. 2015. Atomic force microscopy measurements of bacterial adhesion and biofilm formation onto clay-sized particles. *Sci Rep* 5:16857. <https://doi.org/10.1038/srep16857>.
58. Janshoff A, Neitzert M, Oberdörfer Y, Fuchs H. 2000. Force spectroscopy of molecular systems-single molecule spectroscopy of polymers and biomolecules. *Angew Chem Int Ed* 39:3212–3237. [https://doi.org/10.1002/1521-3773\(20000915\)39:18<3212::AID-ANIE3212>3.0.CO;2-X](https://doi.org/10.1002/1521-3773(20000915)39:18<3212::AID-ANIE3212>3.0.CO;2-X).